

Redox Chemistry

The Effect of pH and Biogenic Ligands on the Weathering of Chrysotile Asbestos: The Pivotal Role of Tetrahedral Fe in Dissolution Kinetics and Radical Formation

Martin Walter,^[a] Walter D. C. Schenkeveld,^{*,[a, d]} Michael Reissner,^[b] Lars Gille,^[c] and Stephan M. Kraemer^[a]

Abstract: Chrysotile asbestos is a soil pollutant in many countries. It is a carcinogenic mineral, partly due to its surface chemistry. In chrysotile, Fe^{II} and Fe^{III} substitute Mg octahedra (Fe[6]), and Fe^{III} substitutes Si tetrahedra (Fe[4]). Fe on fiber surfaces can generate hydroxyl radicals (HO[•]) in Fenton reactions, which damage biomolecules. To better understand chrysotile weathering in soils, net Mg and Si dissolution rates over the pH range 3.0–11.5 were determined in the presence and absence of biogenic ligands. Also, HO[•] generation and Fe bulk speciation of pristine and weathered fibers were examined by EPR and Mössbauer spectroscopy. Dissolution rates were increased by ligands and inversely related to pH with complete inhibition at cement pH (11.5). Surface-

exposed Mg layers readily dissolved at low pH, but only after days at neutral pH. On longer timescales, the slow dissolution of Si layers became rate-determining. In the absence of ligands, Fe[6] precipitated as Fenton-inactive Fe phases, whereas Fe[4] (7 % of bulk Fe) remained redox-active throughout two-week experiments and at pH 7.5 generated 50 ± 10 % of the HO[•] yield of Fe[6] at pristine fiber surfaces. Ligand-promoted dissolution of Fe[4] (and potentially Al[4]) labilized exposed Si layers. This increased Si and Mg dissolution rates and lowered HO[•] generation to near-background level. It is concluded that Fe[4] surface species control long-term HO[•] generation and dissolution rates of chrysotile at natural soil pH.

Introduction

Asbestos is a generic term for silicate minerals with a fibrous crystal habit used in technical applications, which includes five amphiboles and one serpentine mineral (chrysotile).^[1] Due to its favorable properties in terms of heat resistance, noncom-

bustibility, and exceptional tensile strength,^[2] asbestos has been used, for example, in roofing, thermal and electrical insulation, cement pipe and sheet, flooring, and coatings.^[3] The use of asbestos has largely been banned in EU countries since the late 1980s because of adverse health effects on fiber inhalation.^[4] In northern America its use has not been banned yet^[4] and in some Asian countries it is even increasing.^[5] Asbestos can cause diseases such as pulmonary fibrosis and asbestosis, carcinoma of the lung, and mesothelioma in the pleura.^[1b,3,6] The health risks of asbestos are primarily related to the persistence, fibrous morphology, and redox reactivity of the fibers on inhalation. The persistence results from slow chemical dissolution and low excretion rates of fibers due to their size and shape.^[6b,7] The redox reactivity of the fibers is largely related to iron at the mineral surface, which can participate in Fenton-like redox reactions generating reactive oxygen species (especially the hydroxyl radical HO[•]) and reactive nitrogen species.^[6b] These radicals may damage DNA, proteins, and lipids.^[8] Each year, more than 100 000 people die from asbestos-related diseases.^[9] Furthermore asbestos is involved in the pathology of 8–15 % of lung carcinomas and nearly all pleural mesotheliomas.^[6a] The WHO-IARC defines all asbestos minerals as carcinogenic to humans (group 1).^[10]

Asbestos contamination in buildings and engineered environments has received most attention, but natural environments may also be contaminated, either geogenically^[11] or anthropogenically, with loose asbestos (e.g., in the vicinity of

[a] M. Walter, Dr. W. D. C. Schenkeveld, Prof. S. M. Kraemer
Department of Environmental Geosciences
University of Vienna, Althanstrasse 14 (UZA II), 1090 Vienna (Austria)
E-mail: w.d.c.schenkeveld@uu.nl

[b] Assoc. Prof. M. Reissner
Institute of Solid State Physics, TU Wien
Wiedner Hauptstrasse 8–10, 1040 Vienna (Austria)

[c] Assoc. Prof. L. Gille
Institute of Pharmacology and Toxicology
University of Veterinary Medicine, Vienna
Veterinärplatz 1, 1210 Vienna (Austria)

[d] Dr. W. D. C. Schenkeveld
Current address: Copernicus Institute of Sustainable Development
Faculty of Geosciences, Utrecht University
Princetonlaan 8A, 3584 CB Utrecht (The Netherlands)

Supporting information and the ORCID identification number(s) for the author(s) of this article can be found under:
<https://doi.org/10.1002/chem.201804319>.

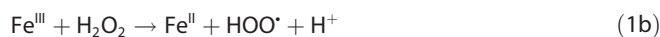
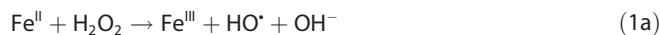
© 2018 The Authors. Published by Wiley-VCH Verlag GmbH & Co. KGaA.
This is an open access article under the terms of Creative Commons Attribution NonCommercial-NoDerivs License, which permits use and distribution in any medium, provided the original work is properly cited, the use is non-commercial and no modifications or adaptations are made.

former asbestos mines or processing sites)^[3,12] or asbestos-containing waste.^[3,13] Thereby, environmental exposure to asbestos increases the incidence of asbestos-associated diseases in exposed residents and causes approximately 400 casualties each year worldwide.^[9] Many countries struggle with environmental asbestos pollution: according to the U.S. EPA, the release of friable asbestos into air, water, and soil was 6.2×10^6 kg in 1999 (from 86 facilities) and 4.0×10^6 kg in 2009.^[10,14] In the vicinity of a former cement plant in western Galilee (Israel), 72 public areas and an estimated 150 000 m³ of soil were polluted with industrial asbestos waste, which necessitated remediation at a total cost of 85 million dollars.^[15] Near the city of Goor in the Netherlands, widespread pollution by friable and nonfriable waste products from an asbestos cement plant was present, which was used to harden dirt tracks, yards, and driveways during 1935–1974.^[13a] This was expected to cause several cases of excess malignant mesothelioma each year. A similar use of asbestos waste products and related increases of asbestos associated diseases was reported for Italy^[13c,d] and in Poland.^[13b]

In industrial applications, mainly chrysotile asbestos has been used (up to 95 %),^[16] and, as a consequence, this mineral is also most commonly encountered in soils contaminated with asbestos. For this reason, we focused on chrysotile asbestos in this study. Chrysotile [Mg₃Si₂O₅(OH)₄] consists of octahedral magnesium hydroxide and tetrahedral silicon oxide layers, which bundle together as a fiber in which Mg hydroxide layers form the external surface.^[17] The dissolution of chrysotile has been extensively studied. Freshly suspended chrysotile has a positively charged surface below pH 8.9, but charge reversal occurs when the outer Mg layer dissolves and the negatively charged Si layer is exposed.^[17a] Dissolution rates are inversely related to pH;^[18] for example, from pH 7 to 10 the Mg dissolution rate was reported to scale with [H⁺]^{0.24}.^[18a] Over a broader pH range (pH 2–8), dissolution rates of Mg and Si were reported to scale exponentially with pH.^[18e] Organic chelators such as oxalate, which are commonly observed in soils^[19] and were found to be exuded by lichens and fungi in contact with asbestos,^[20] enhance Mg dissolution rates of asbestos^[18d] at acidic and mildly acidic pH values.^[18a,d] In soil environments, rates of mineral weathering processes depend on specific chemical conditions. The presence of cement in asbestos cement waste locally buffers soil pH in the highly alkaline pH range and is also expected to affect weathering rates.

Because of the risk associated with Fe, its dissolution behavior from chrysotile deserves specific attention. Fe is substituted into chrysotile during petrogenesis (usually ≈ 2–3 wt %).^[21] Ferrous and ferric Fe are substituted in Mg octahedra (Fe^{II}[6] and Fe^{III}[6]), whereas only ferric Fe is substituted in Si tetrahedra^[22] (Fe^{III}[4]), even though the ionic radius of Fe^{III}[4] (49 pm) is approximately twice as large as the ionic radius of Si^{IV}[4] (26 pm).^[23] In the circumneutral pH range and in the presence of oxygen, Fe release from the chrysotile lattice is coupled to the precipitation of secondary Fe(hydr)oxide minerals with very low solubility. Therefore, net Fe mobilization only occurs in the presence of chelators such as the bacterial siderophore desferrioxamine B (DFOB), citrate, and synthetic chelators such as EDTA.^[1b,24] Fe mobilization from fibers in vivo at pH 7.4 has

been documented and was presumably caused by formation of soluble chelate complexes.^[25] The abundance of reactive Fe sites on chrysotile surfaces can be correlated with the HO[•] yield of the fibers (i.e., their potential to form hydroxyl radicals), under the assumption that Fe at the surface can be repeatedly oxidized and reduced in a Haber–Weiss cycle, as demonstrated for amphibole asbestos^[1b,26] [Eqs. (1 a) and (1 b)]:



The HO[•] yield of fibers decreases when Fe at reactive sites is removed from the fiber surface by ligand-promoted dissolution^[20b,27] and when it precipitates as Fenton-inactive Fe(hydr)oxide minerals during dissolution of the fibers.^[20b] Both processes have only been observed at selected pH values (especially at physiological pH 7.4) or in unbuffered solutions.^[20b] Al is the second most abundantly substituted metal in chrysotile (the Al₂O₃ content of UICC chrysotile is between 0.5 and 1 %).^[21] Like Fe, Al is substituted into octahedral and tetrahedral positions in chrysotile; octahedrally coordinated Al is usually more abundant than tetrahedrally coordinated Al (Al^{III}[4]).^[28] The dissolution of Al from mineral surfaces is also enhanced by ligands such as oxalate and DFOB.^[29] Many reported studies on chrysotile dissolution have provided valuable insight into the geochemistry of asbestos, but it is difficult to translate their findings to environmental systems such as soils. These include not only acid-leaching studies,^[30] but also dissolution studies in which the pH was not^[18c,20b] or insufficiently buffered.^[18d] In some studies very high ligand concentrations were used^[18d] or pH buffering was done with metal chelators^[18b] [e.g., (2-amino-2-(hydroxymethyl)propane-1,3-diol (Tris) or citrate]^[24a,31] without taking into account the effect of these ligands on chrysotile dissolution. Overall, the effect of biogenic ligands on chrysotile dissolution rates and fiber reactivity has not yet been investigated in a comprehensive way over the environmentally and physiologically relevant pH range. Particularly the roles of Fe and Al have only been marginally addressed in this context.

The aim of the present study was to explore how biogenic ligands affect the weathering rates and radical generation over an environmentally and physiologically relevant pH range, and to identify the role of Fe and Al in fiber dissolution kinetics and redox reactivity. Substitution of foreign metals into crystal lattices is known to increase dissolution rates of minerals, for example, in the case of Al substitution in Fe(hydr)oxide minerals.^[29a,32] In this context we hypothesized that substituted metals in the Si layers such as Fe and potentially Al may play an important role in long-term dissolution of chrysotile. After fast initial dissolution of the octahedral Mg hydroxide layer (except at alkaline pH), dissolution of Si is considered to be the rate-determining step in overall dissolution.^[18a,b,d,e,30c] We hypothesized that the complexation or hydrolysis of tetrahedrally substituted metal ions may labilize the surface of the Si layer, for example, through formation of surface defects, and thereby accelerate overall chrysotile dissolution rates. A similar labiliza-

tion of Si lattices by proton- and ligand-promoted Al dissolution has been observed in feldspars.^[29b] Furthermore, we hypothesized that Fe^{II}[6] contributes little to the long-term Fenton activity on dissolving fiber surfaces due to rapid precipitation as secondary Fenton-inactive Fe minerals during fast Mg dissolution. Since Si dissolution is comparatively slow, we hypothesized that Fe^{III}[4] is the only relevant long-term Fenton-active radical-forming Fe species in chrysotile. These hypotheses were tested in batch dissolution experiments with subsequent analysis of metal concentrations in solution [inductively coupled plasma optical emission spectrometry (ICP-OES)], HO[•] yield (EPR spectroscopy), and Fe speciation in the fibers (⁵⁷Fe Mössbauer spectroscopy).

Results and Discussion

Magnetite and chlorite contamination in Shijiazhuang chrysotile asbestos

This study addresses the role of Fe in the dissolution and redox reactivity of chrysotile. Therefore, Fe from impurities in chrysotile asbestos could potentially compromise the interpretation of the results of the experiments. Hence, we first assessed these Fe-containing impurities. Magnetite (Fe₃O₄) is a common impurity in chrysotile asbestos;^[22a] for example, approximately 60% of the bulk Fe in Canadian UICC chrysotile is in magnetite.^[33] After selective removal of visible magnetite particles, analysis of the Mössbauer spectra of pristine Shijiazhuang chrysotile fibers revealed that 32% of bulk Fe was still

in magnetite (Table 1). The potential contribution of magnetite to radical generation and Fe dissolution has been assessed previously. Fubini and Mollo^[34] measured free-radical generation by 45 mg of magnetite [135 arbitrary units (a.u.)] and chrysotile (223 a.u.) with the same specific surface area (27 m²g⁻¹). Furthermore, Fubini et al.^[26a] reported that a 100 mmol L⁻¹ solution of desferrioxamine B (DFOB) buffered at pH 7.4 mobilized 50 μmol L⁻¹ Fe from both 1 g L⁻¹ chrysotile (27 m²g⁻¹) and 1 g L⁻¹ magnetite (21 m²g⁻¹) over 3 d of incubation. Because, normalized to mass, radical formation by and Fe dissolution from magnetite and chrysotile are similar, but the magnetite content of the Shijiazhuang chrysotile asbestos is low (1.5 ± 0.2%) compared to the chrysotile content (86.4 ± 4.6%, by XRD Rietveld refinement), the contribution of magnetite to the HO[•] yield of chrysotile and to Fe dissolution were assumed to be negligible. This assumption was tested in preliminary experiments. The 5,5-dimethyl-1-pyrroline *N*-oxide (DMPO)/HO[•] EPR signal of approximately 1 mg of extracted magnetite (about six times as much as the content expected in the chrysotile samples analyzed by EPR spectroscopy) was only slightly above the background level, and mobilized Fe concentrations from approximately 2 mg of extracted magnetite in 100 mL of 1 mmol L⁻¹ DFOB solution, which corresponds to the density of the magnetite suspension in the chrysotile dissolution experiments, buffered at pH 3.0 for up to 336 h, was below the limit of quantification (LOQ). However, magnetite contamination will affect measurements of total bulk Fe by fusion digestion and neutron activation analysis (NAA).

Table 1. Bulk analysis of pristine and weathered Shijiazhuang chrysotile asbestos. Mean bulk Mg, Si, Fe, and Al contents of Shijiazhuang chrysotile asbestos determined by fusion digestion ($n = 15$) and neutron activation analysis (NAA, $n = 2$). Values in parentheses indicate standard deviations. Results from Mössbauer analysis of pristine fibers and fibers weathered for two weeks at pH 3.0 in a 1 mmol L⁻¹ DFOB or a blank treatment. S1–S3 correspond to the subspectra assigned to chrysotile (Figure 5), values in brackets indicate the Fe coordination. S4 and S5 correspond to the magnetite subspectra (Figure 5); defining parameters for these spectra are presented in Table S7 of the Supporting Information. A ferrihydrite subspectrum (S6; based on data from Murad and Schwertmann^[52]) was added for interpreting the spectrum of the blank treatment (" + FH" in comparison to "original species" without the addition of S6). eQVzz/4 refers to the quadrupole splitting to the center shift relative to ⁵⁷CoRh, and Γ to the line widths. FH indicates ferrihydrite.

Elemental contents of pristine chrysotile [g kg ⁻¹]:					
	Mg	Si	Fe	Al	
fusion digestion	249 (6.8)	188 (3.3)	19.0 (1.4)	8.0 (0.5)	
NAA			21.5 (0.4)		
Fe speciation determined by Mössbauer [%]:					
	eQVzz/4	CS	Γ/2	Fraction in chrysotile	
	[mm s ⁻¹]	[mm s ⁻¹]	[mm s ⁻¹]	[%]	
Pristine					
S1	Fe ^{II} [6]	1.29	1.05	0.22	38
S2	Fe ^{III} [6]	0.33	0.19	0.38	55
S3	Fe ^{III} [4]	0.22	0.09	0.3	7
				Total bulk Fe in chrysotile:	68
DFOB-altered					
S1	Fe ^{II} [6]	1.29	1.05	0.22	38
S2	Fe ^{III} [6]	0.33	0.19	0.38	55
S3	Fe ^{III} [4]	0.22	0.09	0.3	7
				Total bulk Fe in chrysotile:	68
Blank-altered					original species
S1	Fe ^{II} [6]	1.29	1.05	0.22	29
S2	Fe ^{III} [6]	0.33	0.19	0.38	65
S3	Fe ^{III} [4]	0.22	0.09	0.3	6
S6	FH ^[52]	0.355	0.23	0.228	–
				Total bulk Fe in chrysotile:	73
					+ FH
					30
					56
					5
					8
					67

Shijiazhuang chrysotile asbestos further contained larger grains of chlorite, an Al- and Fe-bearing mineral $[(\text{Mg},\text{Fe})_5\text{Al}_2\text{Si}_3\text{O}_{10}(\text{OH})_8]$. The Rietveld fraction of chlorite ($2.4 \pm 2.9\%$) corresponded to $2.3 \pm 2.8 \text{ g kg}^{-1}$ Al. Since 8 g kg^{-1} of Al was determined in chrysotile by fusion digestion, more than 25% was possibly located in chlorite. Furthermore, Fe in chlorite may interfere with dissolution experiments and Mössbauer analysis. The worst-case amount of Fe possibly located in chlorite, assuming that all chlorite in the fibers was chamosite (the Fe end member of the chlorite group), was calculated to be $9.4 \pm 11.3 \text{ g kg}^{-1}$. However, Albino^[35] found a similar Fe content in chlorites as in associated serpentinite minerals. Considering the low chlorite content in our sample, this would point towards a minor contribution of chlorite-associated Fe to the total Fe content. However, Fe partitioning between chlorite and chrysotile may be influenced by the specific conditions during serpentinization.

Dissolution experiments

Net dissolution rates of Si and Mg

To facilitate the comparative discussion of the various treatments, Si and Mg concentration data from all dissolution experiments are presented in Table S1 of the Supporting Information. Consistent with previous observations,^[18a,b,d] net Mg dissolution rates changed systematically over time, with a first stage of rapid dissolution (0.5–8 h), transitioning into a second stage (24–336 h) with slower dissolution (Figure 1a1). The fast Mg dissolution in the first stage (Figure S1 in the Supporting Information) was observed at all pH values except for pH 11.5 (see all rates in Table S2 in the Supporting Information).

The Si mobilization rates decreased much less with incubation time. Hence, only little Si was mobilized during the short first stage of Mg dissolution (Figure 1a2), which was dominated by Mg dissolution from the outermost layer during this stage. Si dissolution rates calculated from blank treatments were well comparable to previously published values^[18a,e] (Figure 1b). However, calculated rates from this study, from Bales and Morgan^[18a] and from Thom et al.,^[18e] were considerably higher than those reported by Rozalen et al.^[18d] This may be explained by a pH drift towards more alkaline conditions in some incubations in the last-named study. Overall, net Si dissolution rates calculated in this study increased with decreasing pH. In the blank and the oxalate treatment, this increase continued down to pH 3.0. In all other treatments, rates only increased down to pH 4.5. On further decreasing the pH to 3.0, the rates remained approximately constant (DFOB) or even declined [citrate and hydroxyethylenediaminetriacetic acid (HEDTA)].

Net Si dissolution rates were generally higher in the presence of ligands than in the corresponding blank treatment over the entire pH range (Figure 1b). The difference was largest for treatments involving chelating ligands with a high affinity for Fe and Al [DFOB, HEDTA, and *N,N'*-di(2-hydroxybenzyl)-ethylenediamine-*N,N'*-diacetic acid (HBED)], even though Si in general forms only complexes having low stability constants

with metal chelates.^[36] From pH 3.0 to 6.0, net Si dissolution rates were highest in DFOB treatments and from pH 7.5–8.5, rates were highest in the HEDTA treatments. Mobilized Si concentrations after 336 h in the HEDTA and DFOB treatments at pH 7.5 and 8.5 were evidently higher than those in all other treatments (Table 2). At pH 11.5, Si was only mobilized in the HBED treatment (Figure 1b; Table S1 in the Supporting Information).

During the slow second stage of Mg dissolution, calculated net Mg dissolution rates were considerably lower than corresponding rates from the first stage (Figure 1c). Calculated rates from blank treatments in this stage were well comparable to previously published values.^[18a,e] However, the rates calculated by Rozalen et al.^[18d] at pH 4.0 were considerably lower. We observed that net Mg dissolution rates during the second stage generally decreased with increasing pH from acidic (3.0) to neutral (7.5) in all treatments (Figure 1c). In the oxalate treatments, the net Mg dissolution rate strongly decreased from pH 3.0 to pH 6.0, and then mildly increased again to pH 7.5. In the pH range of 3.0–7.5, Mg dissolution rates were consistently higher in the presence of hexadentate chelating ligands such as DFOB and HEDTA than in the blank treatment. In the presence of oxalate, Mg dissolution rates increased at low pH, but were inhibited at $\text{pH} \geq 6.0$. Equilibrium modeling indicated undersaturation of Mg oxalate minerals under all experimental conditions, suggesting that net dissolution was not affected by precipitation of Mg oxalate. At pH 7.5 and 8.5, differences in net Mg dissolution rates were small. Under very alkaline conditions (pH 11.5), no Mg was mobilized from the outermost layer, except in the presence of HEDTA, citrate, and HBED (Figure 1c; Table S1 in the Supporting Information). Brucite solubility is very low under such conditions,^[18a,d,37] from the measured Mg concentrations, brucite was predicted to be oversaturated in the blank treatment, but undersaturated in the HBED treatment (Table 3). In fact, equilibrium modeling suggested that the Mg complexes of ligands such as HEDTA, citrate, and HBED dominate Mg solution speciation at such high pH values (data not shown).

Relationship between net dissolution rates and mineral structure

Weathering of chrysotile in the mildly acidic to alkaline pH range is commonly thought of as layer-by-layer dissolution of alternating Mg and Si sheets.^[18a,b] These sheets are bent onto themselves to form needles composed of spirals of Mg and Si layers with the octahedral Mg layer on the convex outer side.^[38] Therefore, the first layer that dissolves from pristine fibers is the outermost Mg hydroxide layer. We interpret the rapid first stage of Mg dissolution to correspond to the fast dissolution of the outer octahedral Mg layer until it is completely removed. Because the first-stage Mg dissolution was fast compared to potential residence times of chrysotile in the environment or in vivo, even at circumneutral pH, its duration can be regarded as negligible. The second stage is characterized by slow, rate-determining dissolution of the tetrahedral Si layer, which then constitutes the mineral surface. The underly-

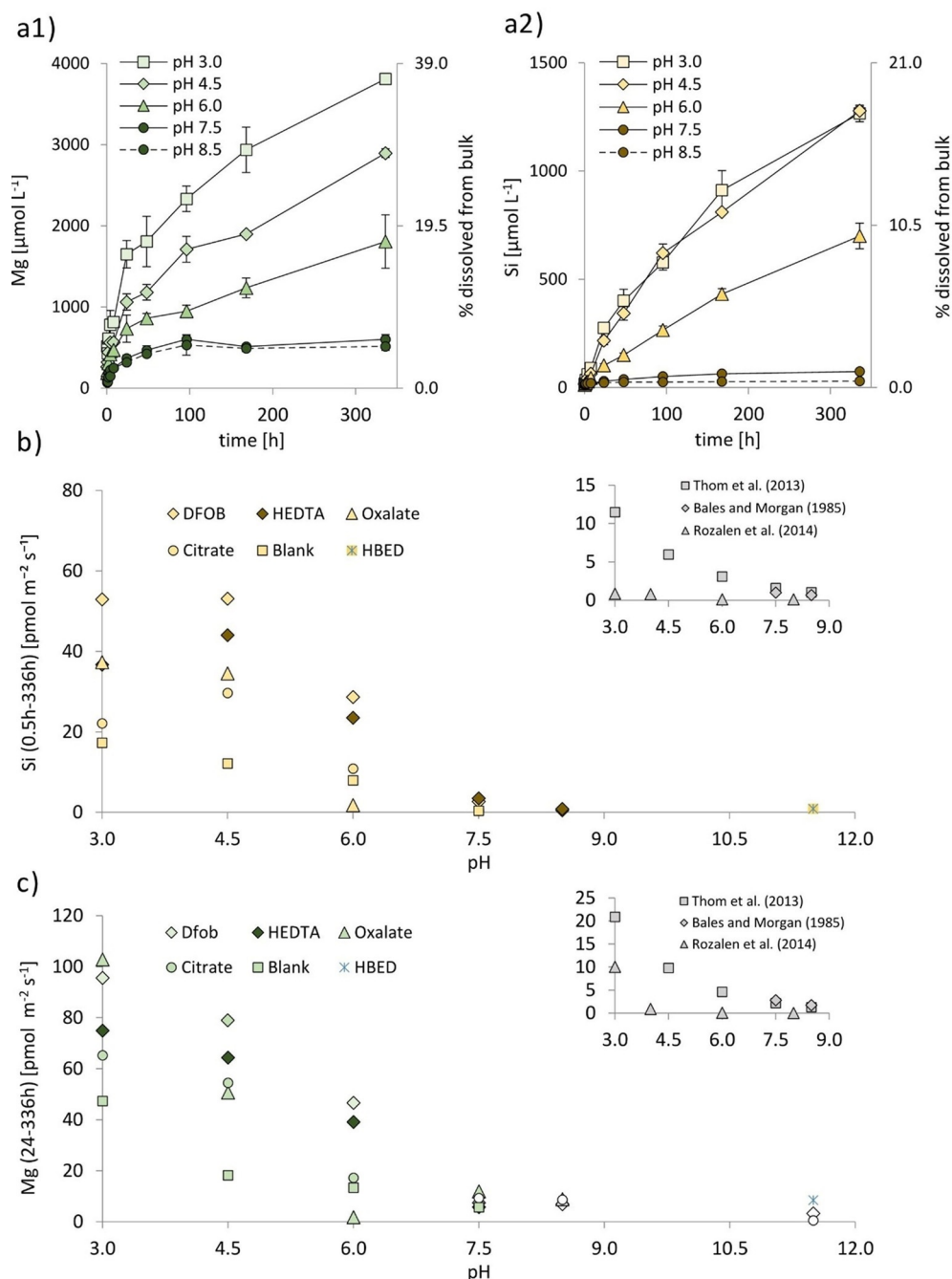


Figure 1. Mg and Si dissolution from 1 g L⁻¹ chrysotile asbestos in blank and 1 mmol L⁻¹ ligand treatments buffered at pH 3.0, 4.5, 6.0, 7.5, 8.5, and 11.5. a1) Mobilized Mg concentrations as a function of time in the presence of 1 mmol L⁻¹ DFOB. Slopes of the first-stage Mg dissolution (0.5–8 h) can be well distinguished from slopes of the second stage (24–336 h). a2) Mobilized Si concentrations from fibers as a function of time in the presence of 1 mmol L⁻¹ DFOB. No dissolution stages were distinguished. In both a1) and a2), the percentage of total bulk dissolution is indicated on the secondary y axis. Error bars indicate standard deviations ($n=2$). Mobilized Mg and Si concentrations as a function of time for all other treatments can be found in Figure S2 of the Supporting Information. b) Si dissolution rates (regression from 0.5 to 336 h). c) Mg dissolution rates calculated for the second stage (regression from 24 to 336 h). Symbols without color filling indicate rates for treatments in which the outermost Mg layer had not completely dissolved after 24 h. Rates of treatments with $R^2 < 0.5$ are not reported. Data included in b) and c) are listed in Table S2 of the Supporting Information. Dissolution rates for blank treatments reported by Bales and Morgan,^[19a] Rozalen et al.,^[19d] and Thom et al.^[19e] are included for comparison in b) and c). Since the pH in the study by Rozalen et al.^[19d] drifted during incubation, the calculated rates were plotted on the initial pH value of the incubation solutions.

ing Mg layer can only dissolve as fast as the removal of the Si layer allows. This is consistent with our observation of more constant Si dissolution rates over time with no distinguishable stages (Figure 1 a2). Equilibrium modeling predictions (Table 3)

suggest that the 1 g L⁻¹ chrysotile suspensions remained undersaturated in all treatments at pH 3.0–8.5 throughout the 336 h of incubation. This is consistent with the literature on even higher suspension densities.^[18a,d] The amount of Mg in

Table 2. Mobilized Mg, Fe, and Si concentrations [$\mu\text{mol L}^{-1}$] after 336 h of incubation at pH 3.0, 7.5, and 8.5. Mobilized Mg concentrations ranged from about 400 to 850 $\mu\text{mol L}^{-1}$, which is within a factor 1–2 compared to the calculated mobilized Mg concentration for complete dissolution of the outermost Mg layer (406 $\mu\text{mol L}^{-1}$). Dissolution of Fe from the outer Mg layer corresponded to Fe concentrations of about $\approx 30 \mu\text{mol L}^{-1}$. This concentration was mobilized after 336 h by DFOB and HEDTA at pH 7.5 and 8.5 and 0.5 h at pH 3.0. After removal of the first Mg layer at pH 7.5 and 8.5, Si mobilization was elevated due to complexation of Fe^{III} [4] and potentially Al^{III} [4] by DFOB and HEDTA, which caused labilization of the Si layer and facilitated Si dissolution. Values in parentheses indicate standard deviations ($n=2$).

	pH 3.0, 0.5 h	pH 7.5, 336 h	pH 8.5, 336 h
First-layer Mg			
blank	552 (144)	585 (105)	448 (22)
DFOB	516 (48)	601 (59)	516 (50)
oxalate	896 (103)	836 (330)	425 (14)
citrate	453 (5)	563 (22)	386 (71)
HEDTA	468 (43)	638 (33)	578 (79)
Fe from first Mg and Si layer			
blank	15.5 (2.4)	0.9 (0.0)	0.1 (0.1)
DFOB	26.1 (1.7)	29.3 (0.2)	30.5 (3.2)
oxalate	36.8 (3.9)	0.1 (0.1)	0.1 (0.0)
citrate	16.4 (0.4)	9.3 (0.5)	4.4 (0.6)
HEDTA	27.4 (2.7)	32.4 (0.5)	33.3 (4.2)
Si dissolution			
blank	11.6 (0.7)	15.4 (0.7)	8.5 (0.2)
DFOB	16.1 (0.5)	73.9 (7.7)	29.5 (1.8)
oxalate	20.7 (1.9)	12.1 (1.3)	11.5 (0.7)
citrate	15.4 (0.1)	22.7 (0.6)	21.6 (0.2)
HEDTA	23.0 (0.0)	101 (3.1)	49.2 (3.9)

the first layer can be estimated from the Mg surface site density of chrysotile (2 nmol cm^{-2})^[18a] and the measured specific surface area of pristine fibers ($20.3 \text{ m}^2 \text{ g}^{-1}$) to be $406 \mu\text{mol g}^{-1}$. However, additional Mg may have dissolved from brucite ($4.5 \pm 2.1\%$ or $771 \pm 360 \mu\text{mol g}^{-1}$ by XRD Rietveld refinement). Due to this uncertainty, it can only be noted that concentrations of dissolved Mg after the fast initial phase of dissolution were approximately within a factor of two compared to the calculated Mg surface layer in all treatments (Figure 1a1; Figure S2 and Table S1 in the Supporting Information). Since in blank treatments hardly any Si dissolved from the fibers up to the first sampling time at pH 3.0 and during the whole incubation

time at pH 7.5–8.5 (Table S1 in the Supporting Information), it can be assumed that only the outermost Mg layer of fibers had dissolved (Table 2).

At pH 3.0–6.0, the relatively quick dissolution of the Si layer enabled faster dissolution of Mg from deeper layers (Figure 1a1). Comparison of the net dissolution rates of Mg and Si during the second stage demonstrates that chrysotile dissolved congruently ($\text{Mg}:\text{Si}=3:2$) at pH 4.5 and 6.0 in all treatments (except in the oxalate treatment at pH 6.0 and citrate treatment at pH 4.5), but incongruently in all treatments at pH 3.0 and most treatments at pH 7.5 and 8.5 (Figure 2a, Table S3 in the Supporting Information). Incongruent dissolution of chrysotile was previously observed in the acidic pH range (below pH 3.0) by Rozalen et al.^[18d] and in the neutral to alkaline pH range by Rozalen et al.^[18d] and Bales and Morgan.^[18a] To examine whether incongruent dissolution at pH 3.0 was caused by precipitation of Si phases, an additional incubation experiment was performed at a lower suspension density of 0.25 g L^{-1} with blank treatment and treatments with 1 mmol L^{-1} DFOB, oxalate, and citrate. Even though dissolution of chrysotile in the blank treatments was closer to congruency than at higher suspension density, rates in the ligand treatments were still far from it (Table S4 in the Supporting Information). Furthermore, already during the first day of incubation at the regular suspension density of 1 g L^{-1} , the concentrations of dissolved Si (below $200 \mu\text{mol L}^{-1}$) were similar or even lower at pH 3.0 compared with pH 4.5. Both observations suggest that precipitation of secondary Si phases is presumably not the cause of incongruent dissolution of chrysotile at pH 3.0. Furthermore, equilibrium modeling predicted (slightly) negative saturation indices for amorphous SiO_2 at pH 3.0–11.5 for Si concentrations mobilized after 336 h by 1 mmol L^{-1} DFOB or HBED (Table 3), the treatments with the highest concentrations of mobilized Si, which supports this argument. Si of the chrysotile structure is known to partly transform into an amorphous siliceous material during dissolution under acidic conditions.^[30a,37] Amorphous silica was primarily observed in alkaline extractions of fibers that had been incubated at pH 3.0 with considerably smaller amounts after incubation at pH 4.5, 6.0, and 7.5 (Figure 2b; Table S3 in the Supporting Information). This is consistent with incongruent fiber dissolution in all treatments at pH 3.0. As the degree of incongruency differed

Table 3. Saturation indices $\text{lg}(\text{IAP}/K_{\text{sp}})$ ^[a] for chrysotile asbestos and secondary minerals that might form during fiber dissolution. Saturation indices were calculated with PHREEQC and the SIT database for pH 3.0–11.5. Mg, Si, Fe, and Al concentrations mobilized after 336 h of incubation in blank (BL) or 1 mmol L^{-1} DFOB (DFOB) treatments at pH 3.0–8.5 and 1 mmol L^{-1} HBED treatments at pH 11.5 were used as input data. The pE was set to equilibrium with air and a temperature of 20°C . Am. ferr. indicates amorphous ferrihydrite, and Am. SiO_2 amorphous SiO_2 .

Phase	Formula	pH 3.0	pH 4.5	pH 6.0	pH 7.5	pH 8.5	pH 11.5 + HBED	pH 11.5 – HBED
chrysotile (BL)	$\text{Mg}_3\text{Si}_2\text{O}_5(\text{OH})_4$	–32.5	–24.5	–16.2	–10.1	–4.9	–5.4	8.9
brucite (BL)	$\text{Mg}(\text{OH})_2$	–14.7	–12.0	–9.1	–6.3	–4.3	–3.2	1.5
Am. SiO_2 (DFOB)	SiO_2	–0.1	–0.1	–0.4	–1.4	–1.9	–4.3	–4.3
Am. ferr. (BL)	$\text{Fe}(\text{OH})_3$	–0.1	1.6					
Am. ferr. (DFOB)	$\text{Fe}(\text{OH})_3$	–8.1	–8.2	–8.3	–8.6	–8.2	–6.6	3.3
diaspore (BL)	$\text{AlO}(\text{OH})$	–4.5	0.6	2.9	2.5	1.6	–0.7	–0.7

[a] IAP: ion activity product.

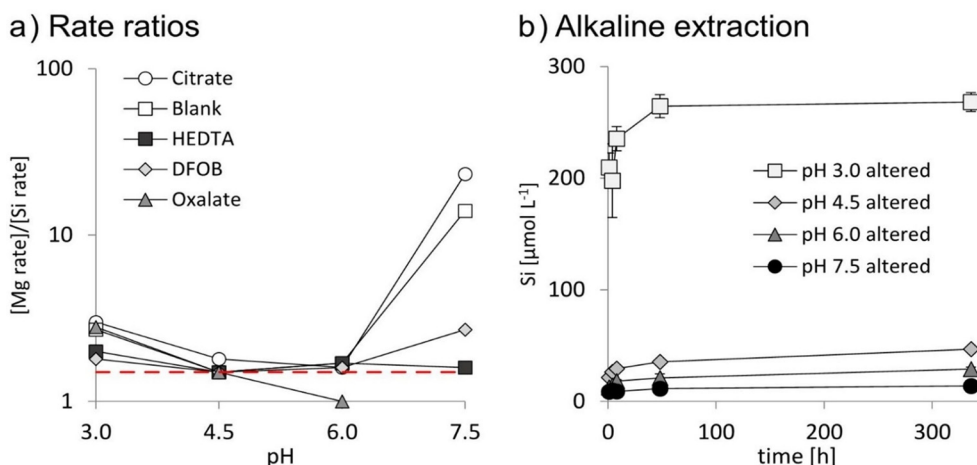


Figure 2. a) Ratios of the Mg and Si dissolution rates of chrysotile shown in Figure 1. The ratio of 1.5 (dashed red line) represents the stoichiometric Mg/Si ratio of chrysotile and hence indicates congruent dissolution. Congruent dissolution was observed in most treatments at pH 4.5 and 6.0. For oxalate, no data point for pH 7.5 was included, because the Si dissolution rate could not be determined at this pH. b) Mobilized Si concentrations extracted in a 0.1 mol L^{-1} NaOH solution from fibers that had been incubated for 336 h at pH 3.0, 4.5, 6.0, and 7.5. Error bars indicate standard deviations ($n=2$).

among the tested treatments (lowest in the DFOB treatment and highest in the citrate treatment, Figure 2a), the formation of the amorphous siliceous materials affected fiber dissolution differently in the different treatments. On the basis of our observations we could not interpret such different effects of the ligands under investigation.

The switch from congruent to incongruent fiber dissolution between pH 4.5 and 3.0 is consistent with the observed incongruent dissolution of chrysotile in simulated phagolysosomal fluids at pH 4.0 in a recent study by Gualtieri et al.^[39] In this study, chrysotile transformed into an amorphous silica-rich fibrous phase. This could provide a possible mechanistic model for the formation of amorphous silica phases observed in our study.

Dissolution of substituted trivalent metals (Fe and Al) and labilization of the Si layer

Figure 3 shows the Fe concentration mobilized from fibers at acidic (3.0), mildly acidic (6.0), mildly alkaline (8.5), and highly alkaline pH (11.5) as a function of time. Fe concentrations mobilized at pH 4.5 and 7.5 are listed in Table S5 of the Supporting Information. In Figure 4, Al mobilization from fibers is shown at pH 3.0, 4.5, 6.0, and 7.5 (Al mobilization was negligible at alkaline pH: Table S6 in the Supporting Information). High concentrations of mobilized Fe and Al are well correlated with high Mg and Si dissolution rates.

At pH 3.0 (Figure 3a), transiently mobilized Fe concentrations in the blank treatment decreased after initial mobilization from $16 \mu\text{mol L}^{-1}$ (0.5 h) to $8 \mu\text{mol L}^{-1}$ (336 h), presumably because of precipitation of secondary Fe minerals on the fiber surface, as observed, for example, by Turci et al.^[20b] The residual Fe concentration of $8 \mu\text{mol L}^{-1}$ after 336 h of incubation corresponds to the Fe^{III} concentrations in solution in equilibrium with ferrihydrite at pH 3.0.^[40] Also, our equilibrium model suggests potential precipitation of amorphous ferrihydrite with a

saturation index close to zero (Table 3). At all pH values above 3.0, the equilibrium models suggest that the mobilized Fe concentrations exclusively resulted from formation of soluble Fe–ligand complexes (data not shown). Unlike the blank treatment, mobilized Fe concentrations at pH 3.0 increased with increasing incubation time in the presence of ligands. At pH 4.5 (Table S5 in the Supporting Information), only submicromolar Fe concentrations were mobilized in the blank treatment. In all other treatments Fe concentrations similarly increased with incubation time, but to a lesser extent than at pH 3.0. At both pH values, DFOB and HEDTA mobilized the highest Fe concentrations. At pH 6.0 (Figure 3b), Fe concentrations in the blank treatment were below the LOQ. In the oxalate treatment they decreased, and this implied depletion of Fe from solution. In the DFOB and HEDTA treatments, mobilized Fe concentrations gradually increased. In the citrate treatment the Fe concentration reached a plateau of about $15 \mu\text{mol L}^{-1}$ after 4 h. Mobilized Fe concentrations at pH 7.5 (Table S5 in the Supporting Information) and 8.5 (Figure 3c) were below the LOQ in the blank and oxalate treatments. In the citrate treatments at pH 7.5 and 8.5, a similar Fe mobilization plateau was observed, albeit after 48 h and at lower concentrations. Fe concentrations mobilized by DFOB and HEDTA increased until 96 h and remained at a plateau of approximately $30 \mu\text{mol L}^{-1}$ until 336 h at both pH values. Presumably, Fe mobilization by these ligands was limited by the slow dissolution kinetics of the first Si layer at pH 7.5 and 8.5, which prevented the ligands from dissolving Fe from deeper layers. A similar amount of Fe was mobilized at pH 3.0 by DFOB, HEDTA, and oxalate within the first 0.5 h, before Si dissolution became substantial (Table 2). We conclude that the $30 \mu\text{mol L}^{-1}$ of Fe mobilized by DFOB and HEDTA mainly represents the Fe content of the outermost Mg layer (Table 2), which was mobilized during the first dissolution stage, with a contribution from the underlying Si layer. This is supported by the relatively high Si concentrations mobilized in the HEDTA and DFOB treatments at pH 7.5 and 8.5

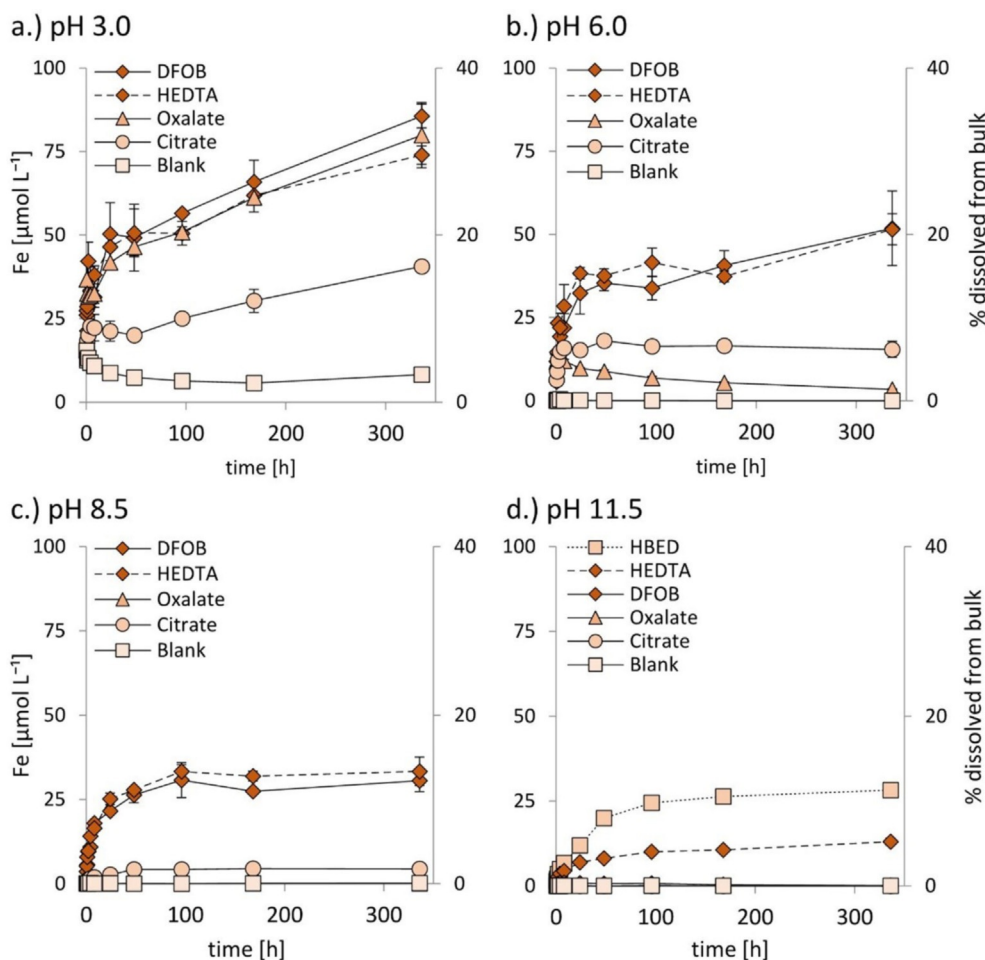


Figure 3. Mobilized Fe concentrations from 1 g L^{-1} chrysotile in blank and 1 mmol L^{-1} DFOB, oxalate, citrate, or HEDTA solutions, buffered at pH 3.0, 6.0, 8.5, and 11.5, and in a 1 mmol L^{-1} HBED solution buffered at pH 11.5. Error bars indicate standard deviations ($n=2$). On the secondary y axis, Fe mobilization is expressed as a percentage of the initial bulk Fe content of chrysotile (the mean of the bulk Fe content determined in fusion digestions and the NAA analysis minus the Fe in magnetite). Data included in this figure are listed in Table S5 of the Supporting Information.

after 336 h (Table 2) compared to the corresponding blank and oxalate treatments. HEDTA and DFOB have a low affinity for Si, but presumably mobilized $\text{Fe}^{\text{III}}[4]$ from the first exposed Si layer and led to labilization of the Si-layer structure by creating crystal defects and corresponding high-energy Si sites. These labile Si sites consequently enhanced Si dissolution rates. The accelerating effect of defect-site generation by removal of Fe from the Si layer on Si-layer dissolution may also operate in the absence of ligands. In this pH range it is more difficult to observe hydrolytic Fe removal from the Si layer, because Fe may be reprecipitated at the mineral surface and thus preclude observation of net mobilization from the silica sheet. However, evidence for changes in speciation of Fe in the solid phase, and therefore support for this mechanism, was gained from measurements of the HO^{\bullet} yield of the fibers (vide infra). At any rate, it is striking that we observed increasing net Si dissolution rates with decreasing pH from 6.0 to 3.0, which could be related to increasing Fe release from the sheet. However, Saldi et al.^[41] also observed increasing dissolution rates of talc (a magnesium silicate) with decreasing pH in the acidic pH range. They attributed this to labilization of partially liberated silica

tetrahedra formed at edge surfaces of talc due to the exchange of Mg^{II} for two protons. Therefore, the pH dependence of net Si dissolution rates cannot unambiguously be attributed to the effect of Fe mobilization from the Si sheet.

A mass balance analysis for the treatments at pH 3.0 after 336 h demonstrated that addition of 1.0 mmol L^{-1} of chelating ligands can result in an increase in mobilized Mg concentration relative to the blank treatment (2.0 mmol L^{-1}) that exceeds the added ligand concentration. This was the case for the DFOB treatment (3.8 mmol L^{-1}) and the oxalate treatment (4.2 mmol L^{-1} ; Table S1 in the Supporting Information). Because Si dissolution is rate-limiting for overall dissolution in the low pH range, the enhanced Mg dissolution resulted from enhanced Si dissolution, due to labilization of the Si layer by ligand-controlled $\text{Fe}^{\text{III}}[4]$ dissolution.

At pH 11.5 (Figure 3d), mobilized Fe concentrations in most treatments were below the LOQ, but in the HEDTA and HBED treatments they increased to 13 and $28 \mu\text{mol L}^{-1}$ after 336 h, respectively. HBED mobilized an amount of Fe corresponding to the estimated Fe content ($\approx 30 \mu\text{mol L}^{-1}$) of the first Mg and Si layers.

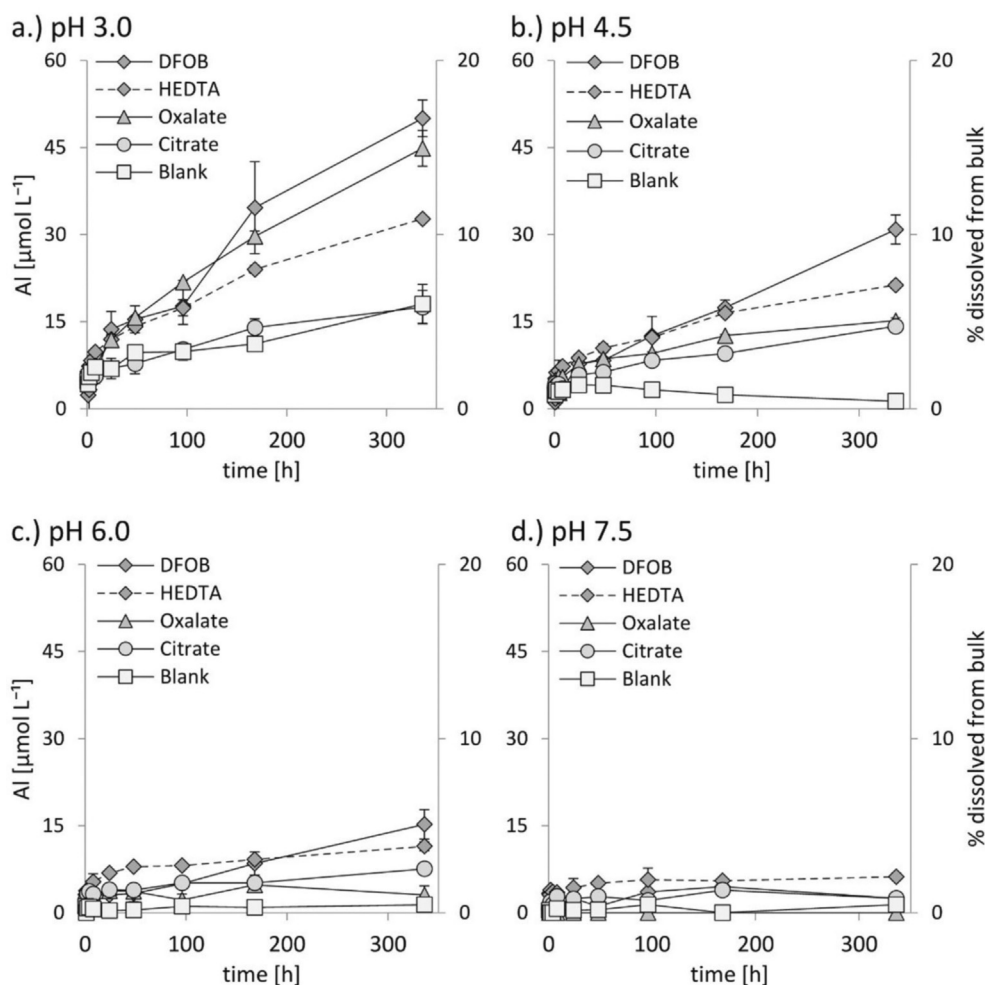


Figure 4. Mobilized Al concentrations from 1 g L^{-1} chrysotile in blank and 1 mmol L^{-1} DFOB, oxalate, citrate, or HEDTA solutions buffered at pH 3.0, 4.5, 6.0, and 7.5. Error bars indicate standard deviations ($n=2$). On the secondary y axis, Al mobilization is expressed as a percentage of the initial bulk Al content of chrysotile. Apart from chrysotile, also some amounts of Al are located in chlorite impurities (discussion in the main text). Data included in this figure is listed in Table S6 of the Supporting Information.

Mobilized Al concentrations at pH 3.0 (Figure 4a) were generally highest in DFOB and oxalate treatments, and lowest in blank and citrate treatments. At pH 4.5 (Figure 4b), Al concentrations in the blank treatment increased until 48 h and subsequently decreased, and this suggested precipitation of an Al-containing phase. Results from equilibrium modeling suggested that secondary Al-containing precipitates such as diaspore [$\alpha\text{-AlO}(\text{OH})$] may form in the blank treatments from pH 4.5 upward (Table 3). In the presence of ligands, however, measured Al concentrations at pH 4.5–7.5 increased over time (except for oxalate at pH 7.5), albeit to a lesser extent than observed at pH 3.0 (Figure 4b–d). Above pH 7.5, a clear increase in mobilized Al concentrations was only observed for DFOB at pH 8.5 and for HBED at pH 11.5 (Table S6 in the Supporting Information).

Since Al can be substituted into the Si layers of chrysotile, ligand- and proton-promoted dissolution of $\text{Al}^{\text{III}}[4]$ may, similarly to the dissolution of $\text{Fe}^{\text{III}}[4]$, contribute to Si labilization in chrysotile. Enhanced Si dissolution rates by the removal of $\text{Al}^{\text{III}}[4]$ have been reported for feldspars.^[29b] Hence, proton-pro-

moted dissolution of $\text{Al}^{\text{III}}[4]$ may have increased Si dissolution from chrysotile at low pH values (Figure 4a and b), whereas ligand-promoted dissolution of $\text{Al}^{\text{III}}[4]$ may have increased Si dissolution over a wider pH range (Figure 4).

Analysis of Mössbauer spectra of weathered fibers

Assuming that hyperfine parameters of chrysotile do not change on weathering, values of the quadrupole splitting, center shift, and line width were obtained that fit well to those reported in literature^[22a] (Figure 5 and Table 1). The relative abundances of $\text{Fe}^{\text{III}}[6]$, $\text{Fe}^{\text{III}}[4]$, and $\text{Fe}^{\text{II}}[6]$ and the fraction of Fe in chrysotile fibers after DFOB treatment corresponded to those of pristine fibers. This suggests that during weathering by DFOB at pH 3.0, no secondary Fe-bearing phases were created. This was not the case for fibers weathered in the blank treatment, for which the relative abundances of the three crystallographic Fe sites differed from those in the pristine fibers (Table 1). The increase in $\text{Fe}^{\text{III}}[6]$ at the expense of $\text{Fe}^{\text{II}}[6]$ in the blank treatment is in agreement with the proposed accumula-

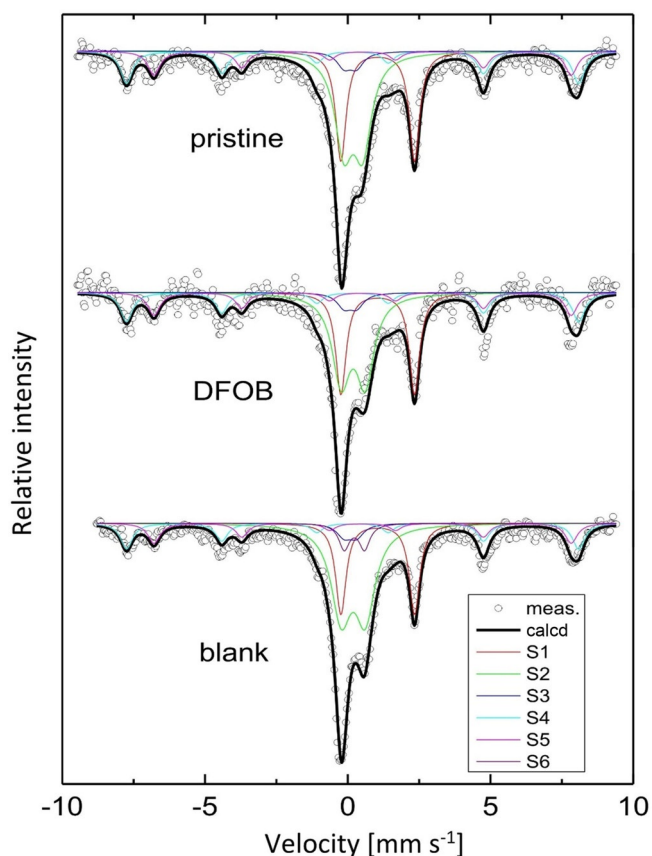


Figure 5. Mössbauer spectra of pristine fibers and fibers weathered for 336 h at pH 3.0 in a blank and 1 mmol L⁻¹ DFOB solution. S1–S3 are subspectra of chrysotile: S1 represents Fe^{II}[6], and S2 and S3 represent Fe^{III}[6] and Fe^{III}[4], respectively. The S4 and S5 subspectra represent Fe in magnetite. In the spectrum of fibers weathered in the blank treatment, a ferrihydrite subspectrum (S6) was added. Center shift data of S1–S3 and S6 are listed in Table 1, and those of S4 and S5 are listed in Table S7 of the Supporting Information.

tion of Fe as Fe^{III}(hydr)oxide minerals on the fiber surface, where Fe^{II}[6] and Fe^{III}[4] were oxidized and/or underwent changes in coordination environment and precipitated as Fe^{III}[6]. By including ferrihydrite in the interpretation of the Mössbauer spectrum obtained for the fibers weathered in the blank treatment, approximately 6% of the bulk Fe was attributed to ferrihydrite (Table 1 and Table S7 in the Supporting Information). This fraction of ferrihydrite approximately corresponds to the theoretical amount of Fe available for precipitation by dissolving Mg and Si layers during incubation (Table S8 in the Supporting Information).

The effect of chrysotile weathering on HO[•] yield

Weathering of chrysotile at different pH values in the presence or absence of Fe-chelating ligands altered the redox reactivity of fiber surfaces to different extents, as quantified by EPR spin trapping (Figure 6). As Fe at the chrysotile surface is largely responsible for the generation of HO[•] from the fibers,^[1b] EPR measurements can assist in linking surface Fe redox reactivity to surface Fe speciation.

Fibers weathered at pH 11.5 in blank, oxalate, citrate, and DFOB treatments had HO[•] yields that differed by less than 15% from that of pristine fibers (100%). This is consistent with marginal Mg and Fe mobilization and suggests (almost) unaltered Fe surface speciation. Among the ligands included in this experiment, only HBED strongly decreased the HO[•] yield of chrysotile fibers at pH 11.5, to 22%; it was also the only ligand that mobilized Fe in concentrations to a substantial degree at this pH (28 μmol L⁻¹). Both at pH 8.5 (75–80%) and at pH 7.5 (60%), the HO[•] yields of fibers weathered in the blank and oxalate treatment were comparable. In both treatments, no Fe was mobilized, but the outermost Mg layer substantially dissolved. Consequently, Fe dissolving from the first Mg layer (≈30 μmol L⁻¹) precipitated as secondary Fe phases on the fiber surface, as supported by dissolution experiments at pH 3.0 and discussed in the context of our Mössbauer spectroscopy observations. Since hardly any Si was mobilized, the coordination of Fe in the first Si layer presumably remained unaltered. Given that the generation of HO[•] radicals by Fe(hydr)oxides is negligible,^[20b,34] the measured HO[•] yields of weathered fibers from the blank and oxalate treatments at pH 7.5 and 8.5 were probably largely caused by Fe^{III}[4] in the exposed Si layer. This demonstrates that the Fe^{III}[4] content of exposed Si layers (which only represented 7.0% of the bulk Fe in chrysotile) gave an HO[•] yield corresponding to about 60% of that generated from the whole exposed Fe[6] pool (HO[•] yield = 100%) in pristine fibers. Assuming the Fe^{III}[4]/Fe^{III}[6] distribution at the surface is the same as in the bulk, this suggests that at the chrysotile surface on average a single Fe[4] center is approximately an order of magnitude more potent than a single Fe[6] center in generating hydroxyl radicals. The HO[•] yield of fibers weathered in the citrate treatments was at both pH values 15–20% higher than in the corresponding blank treatment. This was surprising, since in the citrate treatments, some Fe was mobilized (16 μmol L⁻¹ at pH 7.5 and 8 μmol L⁻¹ at pH 8.5). Because in citrate treatments at neutral pH no substantial mobilized Si concentrations were measured (Table S1 in the Supporting Information), this suggests that citrate complexed Fe[6] from the fiber surface, but not Fe^{III}[4]. The DFOB treatment strongly decreased the HO[•] yield to 17% at pH 8.5 and to 9% at pH 7.5. This can be related to the ability of DFOB to complex most of the Fe from both the Mg and the Si layers (Table 2), leaving an Fe-depleted surface. The lowest HO[•] yield of fibers in the blank treatments were observed at pH 3.0–6.0 (≈40 ± 10%). At these pH values, elevated Si concentrations were measured, which implied dissolution and alteration of the Si-layer structure (but not at pH ≥ 7.5). Assuming that the Fe^{III}[4] content in Si layers at pH 3.0–6.0 was hydrolytically dissolved from Si lattices and only thereafter triggered Si labilization, a Si layer partially depleted in Fe^{III}[4] would consequently form. Partial Fe depletion may explain the lower HO[•] yields of blank fibers incubated at pH ≤ 6.0 relative to those treated at pH 7.5 and 8.5. The nearly two times larger ionic radius of Fe^{III}[4] relative to Si^{IV}[4] could facilitate the hydrolysis of Fe^{III}[4] from Si layers. After dissolution from the Si lattice, Fe^{III}[4] would presumably change its coordination to Fe^{III}[6] in Fe precipitates. This change in coordination was already suggested

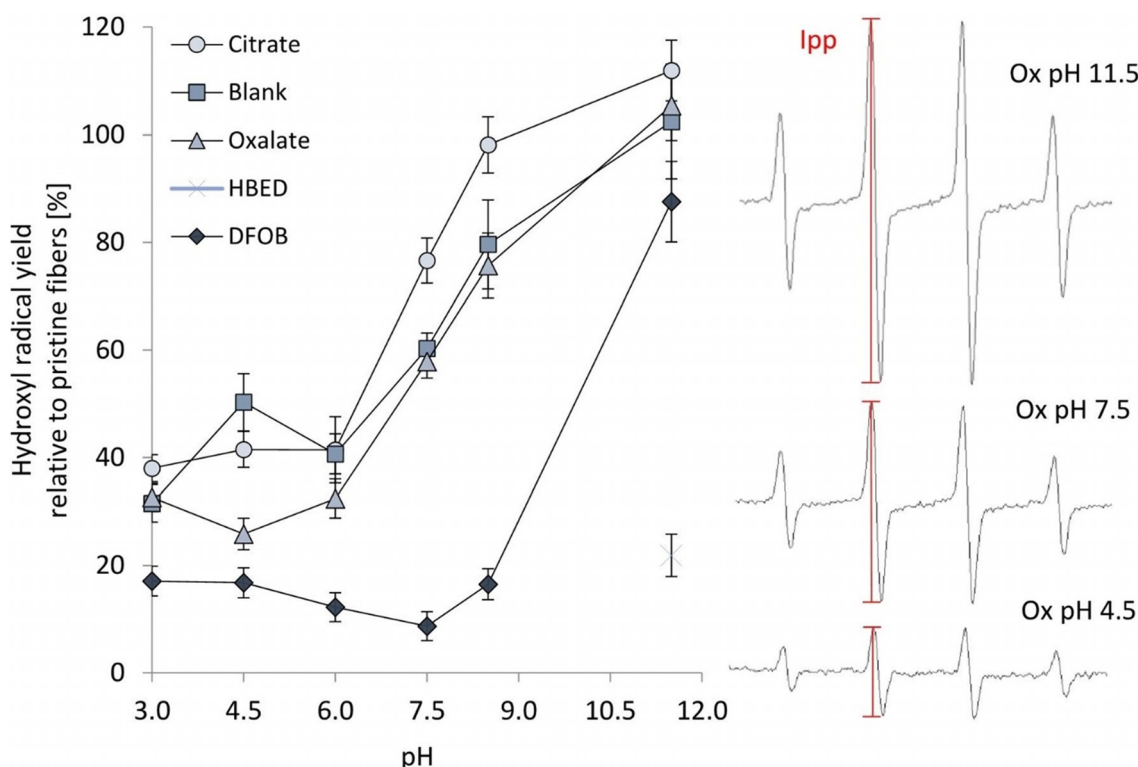


Figure 6. EPR spin-trapping DMPO/ HO^\bullet I_{pp} values of fibers weathered in blank and 1 mmol L^{-1} ligand treatments at various pH values (pH 3.0, 4.5, 6.0, 7.5, 8.5, and 11.5) relative to the I_{pp} value of pristine reference fibers (100%). The incubation time was 336 h. Error bars indicate standard deviations ($n=4$). For visualization, three DMPO/ HO^\bullet spectra of fibers weathered in 1 mmol L^{-1} oxalate treatments at pH 4.5, 7.5, and 11.5 are shown. The I_{pp} value of the second peak from the left (indicated by red bars) was used for determining the peak-to-peak intensity. Data for this figure are listed in Table S10 of the Supporting Information.

on the basis of results from Mössbauer spectroscopy on blank-altered fibers at pH 3.0. Fibers weathered in oxalate and citrate treatments at pH 3.0–6.0 had similar HO^\bullet yields to those measured in the corresponding blank treatments ($\approx 40 \pm 10\%$, except for oxalate treatment at pH 4.5), even though oxalate and citrate mobilized Fe from the fibers in this pH range. Given that only little or no Fe was mobilized in the corresponding blank treatments, the similar HO^\bullet yields of fibers were independent of whether 1) Fe was removed from the fiber surface (oxalate, citrate) or 2) precipitated on the fiber surface (blank). From pH 3.0 to 6.0, mobilized Si concentrations (Table S9 in the Supporting Information) and net Si dissolution rates (Figure 1b) were consistently highest in the DFOB treatments, and this suggests that the kinetics of $\text{Fe}^{\text{III}}[4]$ dissolution from the Si layers by DFOB were faster than in citrate, oxalate, and blank treatments. The faster $\text{Fe}^{\text{III}}[4]$ dissolution kinetics in DFOB treatments may cause relatively fast depletion of $\text{Fe}^{\text{III}}[4]$ from Si layers. This may explain the consistently lower HO^\bullet yields of fibers measured for the DFOB treatment at pH 3.0–6.0 ($\approx 12\text{--}17\%$). The similar HO^\bullet yields in the citrate, oxalate, and blank treatments at pH 3.0 suggest that the $\text{Fe}^{\text{III}}[4]$ dissolution rates were equal in these treatments and that proton-promoted dissolution governed the overall $\text{Fe}[4]$ dissolution rate. The larger Si dissolution rates in the oxalate and citrate treatment compared to the blank treatment at pH 3.0–6.0 (Figure 1b) might be related to enhanced $\text{Al}^{\text{III}}[4]$ dissolution by the ligands.

HO^\bullet yield in relation to fiber weathering kinetics at pH 7.5

The two different modes of decreasing the HO^\bullet yield of fibers (ligand-promoted Fe dissolution and proton-promoted Fe hydrolysis with subsequent precipitation of $\text{Fe}(\text{hydr})\text{oxide}$ minerals on fiber surfaces) have different kinetics and different steady states, as illustrated by the decrease in HO^\bullet yield over time at pH 7.5 in the blank and DFOB treatments (Figure 7). Within 0.5 h, the HO^\bullet yield of fibers in the blank treatment at pH 7.5 had decreased to 77%. After 8 h, it had further decreased to 57%, after which it remained approximately constant ($\approx 50 \pm 10\%$) until 336 h. This indicates that already after 8 h, $\text{Fe}^{\text{III}}[6]$ no longer contributed to the generation of radicals. This supports our hypothesis that $\text{Fe}[6]$ at the surface becomes Fenton-inactive quickly, due to precipitation as hydroxide minerals within hours, whereas $\text{Fe}^{\text{III}}[4]$, which generates the HO^\bullet yield of about $50 \pm 10\%$, remained Fenton-active for the entire incubation time. This implies that $\text{Fe}^{\text{III}}[4]$ is the only relevant long-term Fenton-active Fe surface species in weathered fibers. However, this does not apply to fibers weathered under very alkaline conditions (e.g., fibers embedded in cement), since the Mg layer, and consequently its $\text{Fe}[6]$ content, does not dissolve under these condition. The initial decrease in HO^\bullet generation by the fibers weathered at pH 7.5 in the DFOB treatment was faster than in the blank treatment. Furthermore, the HO^\bullet yield of the fibers did not reach a plateau value during the in-

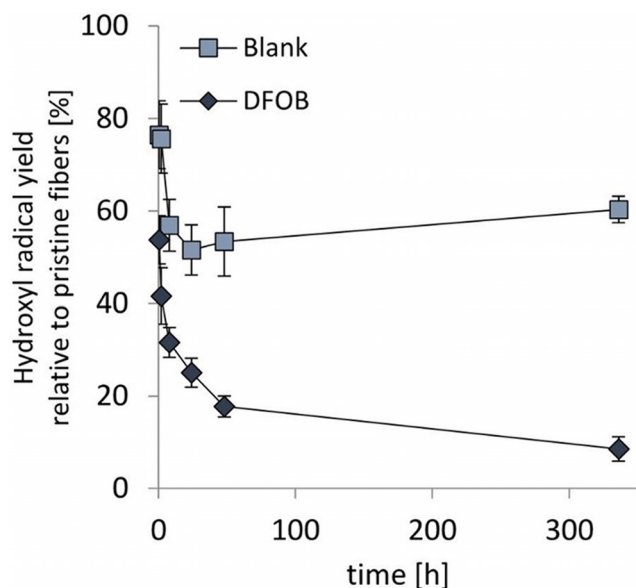


Figure 7. EPR spin-trapping DMPO/HO[•] I_{pp} values of fibers weathered in blank and 1 mmol L^{−1} DFOB treatments at pH 7.5 for 0.5, 2, 8, 24, 48 or 336 h, relative to the I_{pp} value of pristine reference fibers (100%). Error bars indicate standard deviations ($n=4$). Data for this figure are listed in Table S11 of the Supporting Information.

cubation. After 0.5 h, the HO[•] generation had already decreased to 54%, after which it then further decreased gradually to 9% after 336 h. This implies that, even in the presence of a strongly Fe-binding ligand such as DFOB, the depletion of Fe^{III}[4] from Si layers at neutral pH values only occurs on the order of days.

Conclusion

Our results show that, in the long term, Si dissolution is rate-determining for chrysotile weathering in the environmentally relevant pH range (3.0–8.5); at the pH of cement, Mg dissolution is inhibited. Chrysotile dissolved congruently at pH 4.5 and 6.0, but incongruently at pH 3.0 and at pH 7.5 and above. The switch from congruent to incongruent dissolution under acidic pH conditions can be related to the formation of an amorphous siliceous material from the Si layers of chrysotile during weathering. Fe^{III}[4] (and potentially Al^{III}[4]) in the Si layers of chrysotile proved to play an important role in the dissolution kinetics of the fibers, even though its abundance was comparatively low (7.0% of bulk Fe in the fibers). The labilization of Si layers by dissolution of Fe^{III}[4] (and potentially Al^{III}[4]) can strongly enhance Si dissolution rates. Fe^{III}[4] dissolution from Si layers was accelerated by chelating ligands. However, only ligands that can dissolve Fe^{III}[4] may accelerate dissolution rates at circumneutral pH in the environment. In asbestos-contaminated soils with circumneutral pH (e.g., carbonaceous soils), hard Lewis base, hexadentate ligands such as siderophores (e.g., DFOB) and phytosiderophores could potentially increase long-term dissolution rates of chrysotile. However, weaker biogenic ligands such as oxalate, which is, for example, exuded by fungi in contact with chrysotile,^[20c] did not induce

Si labilization at neutral pH and are therefore unlikely to affect overall dissolution rates in such environments. With respect to the radical formation of fibers, our results demonstrate that Fe[6] from the Mg layers loses its ability to generate HO[•] radicals quickly (within hours) over a wide pH range due to precipitation of secondary Fe phases with low Fenton activity (as reported in this study and observed, for example, by Turci et al.^[20b]). Given this quick precipitation of Fe[6] during fiber dissolution, complexation of Fe[6] by ligands in soils will in the long run not decrease HO[•] generation by fibers markedly, as shown for instance in citrate treatments at neutral pH. In the long term, Fe^{III}[4] proved to be the only Fenton-active Fe surface species in chrysotile in the natural soil pH range (3–9). At the alkaline pH of cement, Fe[6] did contribute to HO[•] generation of the fibers, as the outermost Mg layer does not dissolve under these conditions. In spite of its low abundance, Fe^{III}[4] in the Si layer exhibited approximately 50 ± 10% of the HO[•] yield of the more abundant Fe[6] in pristine fibers. Turci et al. have shown that HO[•] generation by synthetic, Fe-doped chrysotile nanocrystals^[42] first increased with increasing Fe content (up to 0.67 wt% Fe), but decreased again with further increasing Fe content.^[43] They concluded that isolated Fe in chrysotile is most potent in radical formation. This, on the one hand, may explain the almost negligible HO[•] generation of precipitated Fe(hydr)oxide minerals, and on the other hand supports that even low concentrations of a Fenton-active Fe species may dominate the redox reactivity of the whole fiber, as demonstrated in this study for Fe^{III}[4] in natural fibers. The pivotal role of Fe^{III}[4] in dissolution kinetics and long-term radical generation described herein may also apply to other silicates and their associated pathologies (e.g., amphiboles, silica, zeolites, and asbestiform talcum).

Experimental Section

Materials and characterization of chrysotile asbestos

All chemical reagents were bought in pro analysis quality from VWR (unless otherwise mentioned). Chrysotile asbestos was purchased from Shijiazhuang Mining IMP&EXP Trade Co. LTD, China. XRD Rietveld analysis of approximately 1 g of ground material (3 min in a WC ball mill at 30 strokes per minute) identified chrysotile (86.4 ± 4.6%), brucite (4.5 ± 2.1%), talc (3.4 ± 2.0%), chlorite (2.4 ± 2.9%), magnetite (1.5 ± 0.2%), quartz (1.0 ± 0.2%), and calcite (0.8 ± 0.2%) (Figure S3 in the Supporting Information). Additionally, single fibers were analyzed by Raman spectroscopy and identified as chrysotile (Figure S4 in the Supporting Information). The mean BET surface area of five replicates, determined with seven adsorption points, was 20.3 m² g^{−1} (with a standard deviation (SD) of 0.9 m² g^{−1}). The bulk elemental composition of the chrysotile asbestos (Table 1) was determined by fusion digestion: fibers were mixed with Li₂B₄O₇ in a ratio of 1:9 and melted in Pt crucibles at 1050 °C for 9 min in a Linn high-therm oven. Afterwards the borate melt was dissolved in 1.25 mol L^{−1} trace metal grade HNO₃ by using a magnetic stirrer at 1100 rpm for approximately 1 h. Metal concentrations were analyzed by ICP-OES. For comparison, serpentine reference samples (LGC standards) were also analyzed. Measured oxide contents (and the reported loss on ignition) of 20 replicates added up to 99.6% (± 1.8 SD) of the mass. The bulk Fe con-

tent was additionally analyzed by a NAA for duplicate samples of 100 mg (Table 1). The bulk Fe content determined by fusion digestion ($19.0 \pm 1.4 \mu\text{mol L}^{-1}$ SD) was comparable to the bulk Fe content determined by NAA ($21.5 \pm 0.4 \mu\text{mol L}^{-1}$ SD). For comparison, mobilized metal concentrations in dissolution experiments were also expressed as a percentage of the total Mg, Si, Fe (mean values of fusion digestions and NAA) and Al (fusion digestion) content (Figures 1 a, 3, and 4; Figure S2 in the Supporting Information). Fe bulk speciation and magnetite contamination were determined by ^{57}Fe Mössbauer spectroscopy.

Dissolution experiments

Chrysotile dissolution studies and fiber incubation for alkaline extraction, EPR, and Mössbauer analysis were carried out at a suspension density of 1 g L^{-1} . Fibers were incubated at six pH values (3.0, 4.5, 6.0, 7.5, 8.5, and 11.5) in solutions containing 50 mmol L^{-1} buffer; pH 3.0–8.5 represented the soil pH range, and pH 11.5 represented the alkaline pH of cement (e.g., in asbestos cement waste).^[44] The non-metal-complexing tertiary amine ("Better") buffers^[45] PIPPS (1,4-piperazinedipropylsulfonic acid, at pH 3.0, 4.5, and 8.5), MES (2-(*N*-morpholino)ethanesulfonic acid, at pH 6.0), and MOPS (3-(*N*-morpholino)propanesulfonic acid, at pH 7.5) were used. The buffers maintained the pH within 0.3 pH units from the target value throughout the experiments. At pH 11.5 no buffer was required for this. To avoid differences in ionic strength (IS) between treatments, the IS of all pH treatments was adjusted to 300 mmol L^{-1} by variable NaCl addition depending on the calculated protonation of the buffers. Blank dissolution experiments (only buffer and electrolyte) were compared with dissolution experiments including 1 mmol L^{-1} citrate, oxalate, DFOB (Novartis), HEDTA (Sigma-Aldrich), or HBED (Sigma-Aldrich). HEDTA is a synthetic chelating agent that was used as a proxy for phytosiderophores, because it has the same functional groups and comparable affinity for metals. Phytosiderophores are exuded by grasses for Fe acquisition and can mobilize Fe and a range of other metals from soil.^[46] HBED is a synthetic ligand with a very high affinity for Fe that is used in Fe fertilizers.^[47] Dissolution studies were carried out in duplicate. Pristine fibers were incubated in 15 mL PP tubes (VWR) for ten incubation times (0.5, 1, 2, 4, 8, 24, 48, 96, 168, and 336 h) in pH-adjusted IS buffer containing 1 mmol L^{-1} citrate, oxalate, DFOB, HEDTA, HBED, or no ligand (blank). Experiments with HBED were done exclusively at pH 11.5. Samples were kept in an end-over-end shaker at 15 rpm and $20 \pm 2^\circ\text{C}$ in the dark.

Solution and fiber sampling was done destructively. Suspensions were filtered through $0.45 \mu\text{m}$ Sartorius cellulose acetate syringe filters. Aliquots of the filtrate were acidified with trace-metal-grade HNO_3 to 0.14 mol L^{-1} . Fibers were sampled by vacuum filtration in Büchner funnels equipped with $0.47 \mu\text{m}$ Nylon membranes (Magna) and washed with ultrapure water to remove adsorbed free ligands and metal complexes. Afterwards, fibers were dried and stored in an evacuated desiccator until analysis. Metal and Si concentrations in the solution samples were analyzed by ICP-OES (Optima 5300-DV, PerkinElmer). The calibration standards were matrix-matched with the samples. All mobilized Si + Mg, Fe, and Al concentrations can be found in Tables S1, S5, and S6, respectively, in the Supporting Information.

Net dissolution rates of Mg and Si were calculated by dividing the slopes of linear regression lines of mobilized concentrations as a function of time by the BET surface area of the pristine fibers. Almost all R^2 values of linear regressions for determining the rates at pH 3.0–6.0 were greater than 0.9, whereas R^2 values of rates calculated at circumneutral pH were lower. Rates were not reported

for experiments with R^2 values < 0.5 . For Si, all dissolution data were used to accomplish this (Figure 1 b). For Mg dissolution rates, two stages were distinguished (Figure 1 c). The first-stage net dissolution rates were calculated from data for the first five time points (0.5–8 h). The second stage net dissolution rates were calculated by using data for $t > 8$ h, if the concentration in all data points was higher than $406 \mu\text{mol L}^{-1}$ (the rationale for this criterion was discussed above).

Alkaline extraction of preconditioned fibers:

Chrysotile fibers were incubated for 336 h at pH 3.0, 4.5, 6.0, and 7.5 in blank solutions and sampled by vacuum filtration. The vacuum-dried fibers were then re-suspended to a suspension density of 1 g L^{-1} in 0.1 mol L^{-1} NaOH solution to extract amorphous siliceous materials, as similarly performed by Clark and Holt.^[37] Extraction times were 1, 4, 8, 48, and 336 h.

Equilibrium modeling

The chemical equilibrium modeling program PHREEQC^[48] and the SIT database were used to assess the solution saturation state of secondary minerals that could potentially precipitate during dissolution experiments. The Mg, Si, Fe, and Al concentrations mobilized after 336 h of incubation, the pH, the electrolyte concentrations, and the ligand concentration (1 mmol L^{-1}) were used as input data. The pH was varied from 3.0 to 11.5. The temperature was set to 20°C and the pE value was adjusted to be in equilibrium with atmospheric oxygen at the respective pH values. Modeling results are listed in Table 3.

Mössbauer measurements

Pristine and altered fibers were analyzed by ^{57}Fe Mössbauer spectroscopy at room temperature in standard constant-acceleration mode with a $^{57}\text{CoRh}$ source, relative to which all center shift data are given. Altered fibers had been exposed to a pH 3.0 buffered solution without (blank) or with addition of 1 mmol L^{-1} DFOB in 500 mL LDPE containers for 336 h (mobilized metal concentrations are listed in Table S9 of the Supporting Information). Fibers were vacuum dried and ground in a tungsten carbide ball mill for 30 s (a time that was shown not to affect $\text{Fe}^{\text{II}}/\text{Fe}^{\text{III}}$ ratios in minerals)^[49] at 30 strokes per minute to avoid spatial anisotropy of fibers in specimens. Fibers (500 mg) were then pressed between Teflon foils (Zuma) and analyzed. The spectra were analyzed by solving the full Hamiltonian. Thickness of the samples was taken into account after Mørup and Both.^[50] All defining parameters for the Mössbauer spectra are presented in Table S7 of the Supporting Information.

EPR spin-trapping measurements

Pristine fibers were incubated for 0.5, 2, 8, 24, 48, or 336 h in 50 mL PP tubes (Greiner Bio-One) at pH 3.0–11.5 in the absence (blank) or presence of 1 mmol L^{-1} ligands (DFOB, oxalate, citrate, and HBED), as described under dissolution experiments. HO^\bullet generation by pristine and altered fibers through Fenton-like redox reactions in the presence of H_2O_2 and 5-5'-dimethyl-1-pyrroline-*N*-oxide (DMPO) as spin trap was determined with an X-band EPR spectrometer (Bruker EMX) and a split ring resonator (Bruker MD5). This technique has frequently been used in this context.^[8b, 20b, 26a, 34, 51] Fibers (11 mg) were incubated for 0.5 h in 0.5 mL of a 125 mmol L^{-1} H_2O_2 and 12.5 mmol L^{-1} DMPO solution buffered at pH 7.4 with a 250 mmol L^{-1} Chelex-treated phosphate buffer. After incubation and centrifugation (5 min with 14000 rpm at room tem-

perature), 50 μL of the supernatant was aspirated into a glass capillary (intraMark Blaumann) and subsequently sealed with Critoseal. Then, the capillary was transferred into the resonator and the EPR measurements were started with the following parameters: microwave frequency 9.6856 GHz; microwave power 20 mW, modulation frequency 100 kHz; modulation amplitude 2 G; time constant 0.327 s; center field 3449 G; scan rate 36 G min⁻¹; sweep width 100 G; scan time 168 s; attenuation 3.17×10^5 ; one scan. EPR measurements were done in quadruplicate. To quantify the change in the HO[•] yield of fibers, the signal intensity (peak-to-peak intensity I_{pp}) of altered fibers was expressed as a percentage of I_{pp} of pristine fibers, which was measured as a reference in each measurement session. Intensities of DMPO/HO[•] spectra were quantified by the height of the second peak from the left in the quadruplet (Figure 6). Mobilized metal concentrations during fiber incubation for EPR measurements are reported in Table S9 of the Supporting Information.

Acknowledgements

We gratefully thank Wolfgang Obermaier for technical support, Dr. Dieter Mader for carrying out the NAA analysis, Andreas Attac MSc for carrying out the Raman analysis, Dr. Christian Lengauer for the XRD Rietveld analysis, and Gino Smeulders for his contribution to the initiation of this project. This work was supported by a uni:docs scholarship of the University of Vienna.

Conflict of interest

The authors declare no conflict of interest.

Keywords: asbestos • iron • radical reactions • redox chemistry • silicates

- [1] a) H. Catherine, W. Skinner, *Indoor Built Environ.* **2003**, *12*, 385–389; b) J. A. Hardy, A. E. Aust, *Chem. Rev.* **1995**, *95*, 97–118.
- [2] H. Schreier, Vol. *Studies in environmental science* 37, Elsevier, Amsterdam, **1989**.
- [3] B. Liu, M. van Gerwen, S. Bonassi, E. Taioli, *J. Thorac. Oncol.* **2017**, *12*, 1031–1045.
- [4] K. Nishikawa, K. Takahashi, A. Karjalainen, C. P. Wen, S. Furuya, T. Hoshuyama, M. Todoroki, Y. Kiyomoto, D. Wilson, T. Higashi, M. Ohtaki, G. W. Pan, G. Wagner, *Environ. Health Perspect.* **2008**, *116*, 1675–1680.
- [5] G. V. Le, K. Takahashi, E. K. Park, V. Delgermaa, C. Oak, A. M. Qureshi, S. M. Aljunid, *Respirology* **2011**, *16*, 767–775.
- [6] a) X. Baur, *Pneumologie* **2016**, *70*, 405–412; b) D. W. Kamp, S. A. Weitzman, *Thorax* **1999**, *54*, 638–652.
- [7] a) B. T. Mossman, A. Churg, *Am. J. Respiratory and Critical Care Medicine* **1998**, *157*, 1666–1680; b) A. Churg, *Ann. Occup. Hyg.* **1994**, *38*, 625–633.
- [8] a) D. W. Kamp, P. Graceffa, W. A. Pryor, S. A. Weitzman, *Free Radical Biol. Med.* **1992**, *12*, 293–315; b) E. Gazzano, F. Turci, E. Foresti, M. G. Putzu, E. Aldieri, F. Silvagno, I. G. Lesci, M. Tomatis, C. Riganti, C. Romano, B. Fubini, N. Roveri, D. Ghigo, *Chem. Res. Toxicol.* **2007**, *20*, 380–387; c) H. Iguchi, S. Kojo, M. Ikeda, *J. Appl. Toxicol.* **1996**, *16*, 309–315; d) I. Fenoglio, L. Prandi, M. Tomatis, B. Fubini, *Redox Rep.* **2001**, *6*, 235–241.
- [9] WHO, International programme on chemical safety: Chrysotile asbestos, ISBN: 978 92 4 156481 6, **2014**.
- [10] WHO-IARC, IARC monographs on the evaluation of carcinogenic risks to humans **2012**, *100 C*, 219–294.
- [11] a) F. Baumann, B. J. Buck, R. V. Metcalf, B. T. McLaurin, D. J. Merkler, M. Carbone, *J. Thorac. Oncol.* **2015**, *10*, 731–737; b) B. J. Buck, D. Goossens, R. V. Metcalf, B. McLaurin, M. Ren, F. Freudenberger, *Soil Sci. Soc. Am. J.* **2013**, *77*, 2192–2204; c) X. L. Pan, H. W. Day, W. Wang, L. A. Beckett, M. B. Schenker, *Am. J. Respiratory and Critical Care Medicine* **2005**, *172*, 1019–1025; d) D. Luce, P. Brochard, P. Quenel, C. Salomon-Nekiriai, P. Goldberg, M. A. Billon-Galland, M. Goldberg, *Lancet* **1994**, *344*, 1777; e) S. Emri, A. Demir, M. Dogan, H. Akay, B. Bozkurt, M. Carbone, I. Baris, *Toxicol. Lett.* **2002**, *127*, 251–257.
- [12] a) K. Anastasiadou, E. Gidararakos, *J. Hazard. Mater.* **2007**, *139*, 9–18; b) C. Mensi, L. Riboldi, S. De Matteis, P. A. Bertazzi, D. Consonni, *Environ. Int.* **2015**, *74*, 191–199; c) C. Magnani, A. Agudo, C. A. González, A. Andron, A. Calleja, E. Chellini, P. Dalmasso, A. Escolar, S. Hernandez, C. Ivaldi, D. Mirabelli, J. Ramirez, D. Turuguet, M. Usel, B. Terracini, *Br. J. Cancer* **2000**, *83*, 104; d) V. Bourdès, P. Boffetta, P. Pisani, *Eur. J. Epidemiol.* **2000**, *16*, 411–417; e) N. Kurumatani, S. Kumagai, *Am. J. Respiratory and Critical Care Medicine* **2008**, *178*, 624–629.
- [13] a) H. A. L. Driece, S. Siesling, P. H. J. Swuste, A. Burdorf, *J. Exposure Sci. Environ. Epidemiol.* **2010**, *20*, 478; b) N. Szeszenia-Dabrowska, U. Wilczyńska, W. Szymczak, K. Laskowicz, *Int. J. Occup. Med. Env.* **1998**, *11*, 171–177; c) D. Ferrante, D. Mirabelli, S. Tunesi, B. Terracini, C. Magnani, *Occup. Environ. Med.* **2016**, *73*, 147–153; d) M. Musti, A. Pollice, D. Cavone, S. Dragonieri, M. Bilancia, *Int. Arch. Occup. Environ. Health* **2009**, *82*, 489–497.
- [14] ATSDR Toxicological Profile for Asbestos, US Department of Health & Human Services, Vol. TP-61, **2001**.
- [15] *Israel Environment Bulletin* Vol. 37, Israel Ministry of Environmental Protection, **September 2011**.
- [16] P. J. Landrigan, *N. Engl. J. Med.* **1998**, *338*, 1618–1619.
- [17] a) R. C. Bales, J. J. Morgan, *Environ. Sci. Technol.* **1985**, *19*, 1213–1219; b) B. W. Evans, *Int. Geol. Rev.* **2004**, *46*, 479–506.
- [18] a) R. C. Bales, J. J. Morgan, *Geochim. Cosmochim. Acta* **1985**, *49*, 2281–2288; b) J. R. Gronow, *Clay Miner.* **1987**, *22*, 21–35; c) I. Choi, R. W. Smith, *J. Colloid Interface Sci.* **1972**, *40*, 253; d) M. Rozalen, M. E. Ramos, S. Fiore, F. Gervilla, F. J. Huertas, *Am. Mineral.* **2014**, *99*, 589–600; e) J. G. M. Thom, G. M. Dipple, I. M. Power, A. L. Harrison, *Appl. Geochem.* **2013**, *35*, 244–254.
- [19] D. R. Kidd, M. H. Ryan, R. E. Haling, H. Lambers, G. A. Sandral, Z. J. Yang, R. A. Culvenor, G. R. Cawthray, A. Stefanski, R. J. Simpson, *Plant Soil* **2016**, *402*, 77–89.
- [20] a) S. E. Favero-Longo, D. Castelli, B. Fubini, R. Piervittori, *J. Hazard. Mater.* **2009**, *162*, 1300–1308; b) F. Turci, S. E. Favero-Longo, M. Tomatis, G. Martra, D. Castelli, R. Piervittori, B. Fubini, *Chem. Eur. J.* **2007**, *13*, 4081–4093; c) S. Daghighi, E. Martino, I. Fenoglio, M. Tomatis, S. Perotto, B. Fubini, *Chem. Eur. J.* **2005**, *11*, 5611–5618.
- [21] D. R. Bowes, C. M. Farrow, *Am. J. Ind. Med.* **1997**, *32*, 592–594.
- [22] a) M. Ristic, I. Czako-Nagy, S. Music, A. Vertes, *J. Mol. Struct.* **2011**, *993*, 120–126; b) G. Stroink, C. Blaauw, C. G. White, W. Leiper, *Can. Mineral.* **1980**, *18*, 285–290.
- [23] R. D. Shannon, *Acta Crystallogr. Sect. A* **1976**, *32*, 751–767.
- [24] a) L. G. Lund, A. E. Aust, *Arch. Biochem. Biophys.* **1990**, *278*, 60–64; b) S. K. Mohanty, C. Gonneau, A. Salamatipour, R. A. Pietrofesa, B. Casper, M. Christofidou-Solomidou, J. K. Willenbring, *J. Hazard. Mater.* **2018**, *341*, 290–296.
- [25] A. Morgan, A. Holmes, C. Gold, *Environ. Res.* **1971**, *4*, 558–570.
- [26] a) B. Fubini, L. Mollo, E. Giamello, *Free Radical Res.* **1995**, *23*, 593–614; b) Z. H. Shen, V. D. Parker, A. E. Aust, *Anal. Chem.* **1995**, *67*, 307–311; c) G. B. Andreozzi, A. Pacella, I. Corazzari, M. Tomatis, F. Turci, *Sci. Rep.* **2017**, *7*, 14696.
- [27] S. A. Weitzman, P. Graceffa, *Arch. Biochem. Biophys.* **1984**, *228*, 373–376.
- [28] C. Viti, M. Mellini, *Eur. J. Mineral.* **1997**, *9*, 585–596.
- [29] a) J. Cervini-Silva, G. Sposito, *Environ. Sci. Technol.* **2002**, *36*, 337–342; b) S. A. Welch, W. J. Ullman, *Geochim. Cosmochim. Acta* **1996**, *60*, 2939–2948.
- [30] a) M. Rozalen, F. J. Huertas, *Chem. Geol.* **2013**, *352*, 134–142; b) F. Wypych, L. B. Adad, N. Mattoso, A. A. S. Marangon, W. H. Schreiner, *J. Colloid Interface Sci.* **2005**, *283*, 107–112; c) A. Morgan, *Ann. Occup. Hyg.* **1997**, *41*, 249–268.
- [31] B. E. Fischer, U. K. Haring, R. Tribolet, H. Sigel, *Eur. J. Biochem.* **1979**, *94*, 523–530.
- [32] S. M. Kraemer, *Aquat. Sci.* **2004**, *66*, 3–18.
- [33] G. Stroink, C. Blaauw, C. G. White, W. Leiper, *Canadian Mineralogist* **1980**, *18*, 285–290.

- [34] B. Fubini, L. Mollo, *Toxicol. Lett.* **1995**, 82–83, 951–960.
- [35] G. V. Albino, *Canadian Mineralogist* **1995**, 33, 559–568.
- [36] G. S. Pokrovski, J. Schott, *Geochim. Cosmochim. Acta* **1998**, 62, 3413–3428.
- [37] S. G. Clark, P. F. Holt, *Nature* **1960**, 185, 237–237.
- [38] A. Baronnet, *Vol. 1*, EMU Notes in Mineralogy, Budapest, **1997**.
- [39] A. F. Gualtieri, S. Pollastri, N. Bursi Gandolfi, M. L. Gualtieri, *Sci. Rep.* **2018**, 8, 7071.
- [40] W. L. Lindsay, *Chemical equilibria in soils*, John Wiley and Sons, N. Y., **1979**.
- [41] G. D. Saldi, S. J. Kohler, N. Marty, E. H. Oelkers, *Geochim. Cosmochim. Acta* **2007**, 71, 3446–3457.
- [42] G. Falini, E. Foresti, M. Gazzano, A. E. Gualtieri, M. Leoni, I. G. Lesci, N. Roveri, *Chem. Eur. J.* **2004**, 10, 3043–3049.
- [43] F. Turci, M. Tomatis, I. G. Lesci, N. Roveri, B. Fubini, *Chem. Eur. J.* **2011**, 17, 350–358.
- [44] D. O. McPolin, P. A. M. Basheer, A. E. Long, K. T. V. Grattan, T. Sun, *J. Mater. Civ. Eng.* **2007**, 19, 936–946.
- [45] A. Kandedgara, D. B. Rorabacher, *Anal. Chem.* **1999**, 71, 3140–3144.
- [46] a) W. D. C. Schenkeveld, Y. Schindlegger, E. Oburger, M. Puschenreiter, S. Hann, S. M. Kraemer, *Environ. Sci. Technol.* **2014**, 48, 12662–12670; b) M. Walter, S. M. Kraemer, W. D. C. Schenkeveld, *Plant Soil* **2017**, 418, 5–23.
- [47] S. López-Rayó, D. Hernandez, J. J. Lucena, *J. Agric. Food Chem.* **2009**, 57, 8504–8513.
- [48] D. L. Parkhurst, C. A. J. Appelo, U. S. Geological Survey Water-Resources Investigations Report, **1999**, pp. 99–4259.
- [49] A. Reay, *Mineral. Mag.* **1981**, 44, 179–182.
- [50] S. Mørup, E. Both, *Nucl. Instrum. Methods* **1975**, 124, 445–448.
- [51] S. Enrico Favero-Longo, F. Turci, M. Tomatis, R. Compagnoni, R. Piervittori, B. Fubini, *J. Toxicol. Environ. Health Part A* **2009**, 72, 305–314.
- [52] E. Murad, U. Schwertmann, *Am. Mineral.* **1980**, 65, 1044–1049.

Manuscript received: August 24, 2018

Revised manuscript received: November 8, 2018

Accepted manuscript online: November 11, 2018

Version of record online: February 4, 2019